HYFI: Hybrid filling of the dead-time gap for faster zero echo time imaging

Romain Froidevaux, Markus Weiger, Manuela B. Rösler, David O. Brunner, Klaas P. Pruessmann

Institute for Biomedical Engineering, ETH Zurich and University of Zurich, Zurich, Switzerland

Corresponding author: Dr. Markus Weiger
Gloriastrasse 35
8092 Zurich, Switzerland
+41 44 632 45 44
weiger@biomed.ee.ethz.ch

Running Title: HYFI

Word count (body text): 4297

Figures + tables: 10

References: 45

Abstract

Purpose: To improve the SNR efficiency of zero echo time (ZTE) MRI pulse sequences for faster imaging of short-T_2 components at large dead-time gaps.

Methods: The HYFI MRI acquisition scheme is described. It retrieves inner k-space data missed during the ZTE dead-time gap arising from radio-frequency excitation and switching. The approach employs hybrid filling of the inner k-space with a small single-point-imaging core surrounded by a stack of shells acquired on radial readouts in an onion-like fashion. Details of the acquisition scheme are presented and a practical implementation of the algorithm is provided. The principles are demonstrated with simulations as well as phantom, in-vitro and in-vivo imaging.

Results: Simulations predict higher SNR efficiency of HYFI compared to PETRA (pointwise encoding time reduction with radial acquisition) at preserved image quality with the advantage increasing with the size of the k-space gap. These results are confirmed by imaging experiments with gap sizes of 25 to 50 Nyquist dwells, in which scan times for similar SNR could be reduced by 25 to 60%.

Conclusion: The HYFI technique provides both high SNR efficiency and image quality, thus outperforming previously known ZTE-based pulse sequences in particular for large k-space gaps. Promising applications include direct imaging of ultra-short T_2 components, such as e.g. the myelin bilayer or collagen, T_2 mapping of ultra-fast relaxing signals, and ZTE imaging with reduced chemical shift artifacts.

Key words: ZTE, PETRA, WASPI, SPI, SNR, short T2

1 Introduction

Direct MRI of tissues with very short transverse relaxation times T_2 or T_2* in the sub-millisecond range such as e.g. bones (1–3), tendons (4–6), brain (7–10), lung (11–13) and teeth (14–16) is receiving increasing attention due to its potential for both clinical diagnosis and basic research. The rapid signal decay of such tissues prevents detection and spatial encoding through conventional echo-based sequences. Therefore, several dedicated short-T2 techniques have been developed, usually avoiding echo formation (17). One efficient and increasingly used technique is zero echo time (ZTE) imaging (18–21) where a frequency encoding gradient is switched on before radio-frequency (RF) excitation and signal is acquired as soon as possible afterwards (Fig. 1a). In this way, 3D k-space is covered with radial center-out trajectories and spherical support (Fig. 1b).

In the ZTE sequence, the dead time Δt caused by RF excitation and switching prevents acquisition of early data, thus leading to a gap in central k-space (20). Hence no data is available in a sphere of radius k_{gap} centered on the k-space origin. To avoid related image artifacts, three approaches have been suggested: Generating the missing information through algebraic reconstruction (22) or recovering it through additional acquisitions using either Cartesian single-point imaging (SPI) (23,24) as proposed for PETRA (pointwise encoding time reduction with radial acquisition) (21) (Fig. 1c) or radial readouts at lower gradient strength as suggested in the WASPI (water- and fat-suppressed proton projection MRI) technique (19) (Fig. 1d).

Algebraic ZTE has the advantages of not requiring additional acquisition and having a benign behavior of the point spread function (PSF) under T_2 decay. However, image reconstruction becomes ill-conditioned for k_{gap} exceeding 3 Nyquist dwells (where a Nyquist dwell is the inverse of the field of view) (25), hence preventing application at larger gaps. WASPI retrieves the missing data with a time-efficient radial acquisition which, however, leads to discontinuous T_2-related modulation transfer function (MTF) in k-space and thus a propensity to large PSF side lobes and associated oscillatory image artefacts (26). On the other hand, PETRA is robust against artifacts but hampered by the slow SPI acquisition of the inner k-space ($k < k_{gap}$) (26). Therefore, the best sequence choice depends on the particular imaging task and especially on the gap size. However, none of the described methods is well suited at large gaps, i.e. k_{gap} being a few tens of dwells, since algebraic ZTE and WASPI lead to poor image quality and PETRA causes undesirably long scan times. Yet, imaging under such conditions can be necessary or beneficial. Indeed, large gaps occur at high imaging bandwidth as required for high-resolution imaging of short-T_2 components, in particular in large field of views (27), or when the dead time is relatively large, either because of limitations of the RF hardware or by choice to enable T_2 selection (21), T_2 mapping, or reduction of chemical-shift artefacts.

To overcome the limitations of ZTE imaging at large k-space gaps, a method dubbed HYFI has been developed (28,29) and was successfully used in a first application (10). HYFI employs a hybrid filling of the gap, thus increasing SNR efficiency as compared to PETRA while largely preserving image

quality. In the present work, this novel technique is described in detail. Both image quality and SNR efficiency are investigated by means of PSF calculations and 3D simulations. The performance of HYFI is demonstrated in several imaging scenarios involving short-T_2 phantoms as well as in-vivo imaging and compared to the PETRA technique.

2 Methods

2.1 Hybrid filling (HYFI)

The basic idea of HYFI is to replace the SPI part in PETRA by a more time-efficient acquisition strategy with a pattern that still avoids strong discontinuities in the MTF as occurring in WASPI. This is accomplished by hybrid filling of the inner k-space with a small SPI core surrounded by a stack of shells acquired on radial readouts in an onion-like fashion (Fig. 1e). To control image quality, large jumps in signal amplitude associated with T_2 decay are avoided by acquiring data over a limited period of time on several radial shells.

Implementation of the described HYFI algorithm is governed by the discrete nature of sampling k-space at Nyquist distance. An example implementation is provided as a Matlab function at the following link. https://doi.org/10.3929/ethz-b-000415045

In more detail, the range R which determines the maximally allowed T_2 decay is defined as

$$R = A \cdot M_T(\Delta t) \quad (1a)$$

where

$$M_T(\Delta t) = \exp(-\frac{\Delta t}{T_2}) \quad (1b)$$

is the amplitude of the transverse magnetization after the dead time, and the decay coefficient

$$A = 1 - \exp\left(-\frac{t_{acq}}{T_2}\right) \quad (1c)$$

is the proportion of signal amplitude consented to be lost during an acquisition duration t_{acq}. In other words, A describes the size of the range R relative to $M_T(\Delta t)$.

A can vary between 0 and 1, corresponding in the limiting cases to PETRA and WASPI, respectively. For a given target T_2, A is chosen to maximally reduce scan time while keeping artifacts to a negligible level. The latter can be evaluated by means of PSF calculations or image simulations, as shown below. t_{acq}, the maximum acquisition duration allowed to limit the decay of a given T_2 to the range R, depends on both the targeted T_2 and the value of A. It can be calculated as derived from Eq. (1c) according to

$$t_{acq} = -T_2 \cdot \ln(1 - A) \quad (2)$$

In general, t_{acq} will be too short to manage acquiring the inner k-space with a single radial spoke. In this case, the inner k-space is split in an onion-like fashion with a core surrounded by one or several shells. Each of these sub-volumes must be acquired within t_{acq} and starting from Δt. Due to the latter, gradient strengths increase linearly with the distance of the first acquired data point from the origin. Whenever, for a gradient strength, more than one data point can be reached during t_{acq}, radial acquisition is performed as in WASPI to optimize scan time, otherwise SPI is used on a Cartesian grid as in PETRA. As a consequence, the core, where low gradient strengths are required, is probed with SPI while all shells are sampled radially. The core radius is

$$k_{SPI} = \frac{\Delta t}{t_{acq}} = \frac{\Delta t}{-T_2 \cdot \ln(1-A)} \qquad (3)$$

where k_{SPI} is given in Nyquist dwells. Theoretically k_{SPI} may reach any value between 0 and ∞ but is practically rounded to integers and limited to the outer limit of the k-space support (c.f. Matlab function). Moreover, it equals $k_{gap} = \Delta t\ BW$ for $A = A_0$, where A_0, the radial onset, is defined by

$$A_0 = 1 - e^{-\frac{\Delta t}{T_2 \cdot k_{gap}}} \qquad (4)$$

For $A < A_0$, $k_{SPI} > k_{gap}$ and the whole inner k-space is acquired with SPI, thus requiring $N_{SPI} = \frac{4}{3}\pi\ k_{gap}^3$ number of RF excitations for Cartesian Nyquist sampling. For $A > A_0$, part of the inner k-space can be acquired radially since $k_{SPI} < k_{gap}$ and less excitations $N_{SPI} = \frac{4}{3}\pi\ k_{SPI}^3$ are needed in the core.

As savings in scan time are largely described by the reduction of the SPI core, Fig. 2a illustrates the effects of the choice of A on N_{SPI}. In typical cases where $\Delta t < T_2$, choosing $A \lesssim 0.1$ is sufficient to decrease the size of the SPI core considerably. Moreover, Fig. 2b shows that in such circumstances the PSF lineshape is largely unaffected (More detailed PSFs are shown in Fig. S1), suggesting that scan time can indeed be reduced while preserving image quality.

Around the core, in each radial shell the angular spoke density is adapted to fulfill the Nyquist criterion at the outer shell radius to minimize scan time. The possible savings in scan time for the complete inner k-space including the acquisition of both core and shells are illustrated in Fig. 3. In the limiting cases of PETRA and WASPI, the number of RF excitations, N_{gap}, required to fill a sphere of radius k_{gap}, varies with the volume and the surface of the sphere respectively. In HYFI, N_{gap} depends on the decay coefficient A and is bounded by these limits. As already suggested in Fig. 2, small decay coefficients are sufficient to significantly decrease N_{gap}.

2.2 Choice of imaging parameters

All imaging parameters are listed in Tab. 1.

Generally, small dead times are desired to maximize signal amplitude and reduce scan duration. However, in some situations it may be preferred to deliberately extend the dead time and/or the gap size. For example, short-T_2 components that cannot be resolved may be selectively suppressed in this way. Moreover, in the inner k-space, data samples are acquired in a small time range bounded by the shell acquisition duration t_{acq}. When t_{acq} is small enough, this leads to similar T_2-weighting and chemical shift-induced phase for all inner k-space data. As a consequence, increasing the inner k-space volume to a substantial part of the support improves the accuracy of T_2 mapping based on a series of such data. In addition, it also reduces PSF blurring (27) and as well as chemical shift artifacts. In this work, increased dead time is employed for suppression of components with extremely short T_2, reduction of chemical shift artifacts, as well as T_2 mapping.

When setting up a protocol, values for target T_2 and decay coefficient A must be selected. A suitable choice of the parameter pair (A, T_2) is crucial for optimal HYFI performance. Figure 2 reveals that a good compromise between image quality and scan time is obtained for $A \lesssim 0.1$. However, in most cases the imaged samples contain multiple signal sources with different relaxation times T_2. Then a choice of A which is appropriate for a given T_2 leads to stronger decay for signals with shorter T_2 and hence potentially to artifacts. As usually not all relaxation times present in a sample are known a priori, an educated choice of the target T_2 may not always be possible. As a rule of thumb, in the presence of multiple T_2s it is considered safe to choose a target $T_2 = \Delta t$ since signals with $T_2 < \Delta t$ will considerably decay before data acquisition. Moreover, as shown in the results section, the target T_2 can be chosen larger than Δt if the MR signal is dominated by sources with $T_2 >> \Delta t$.

2.3 Hardware

All experiments were performed on Achieva MRI systems (Philips Healthcare, Best, Netherlands) at 3 T or 7 T complemented with symmetrically biased transmit-receive switches (30) with switching times of approximately 3 µs at 3 T and 1 µs at 7 T, custom-made spectrometers (31) with up to 4 MHz acquisition bandwidth and short digital filters with group delays down to 1.2 µs. Moreover, the 3 T scanner was equipped with a high-performance gradient insert system capable of reaching 200 mT/m at full duty cycle (32) and a broadband linear RF power amplifier BLA1000-I E (Bruker Biospin, Wissembourg, France) with the advantage of a relatively small ring-down signal (33). Largely 1H-free RF coils were used for both transmission and reception, a surface coil of 80 mm diameter and two birdcage coils (34,35). Block and sweep HSN pulses with bandwidth matching the imaging bandwidth were used for RF excitation.

2.4 Samples

An imaging phantom with two different T_2s was created by placing a stack of erasers with $T_2 \approx 300$ µs onto a disk made of rubber with $T_2 \approx 100$ µs.

A bone phantom was taken from a previous study (26). The piece of bovine tibia of 60 mm diameter and 25 mm thickness had been freed of sources of long-lived MR signal, i.e. soft tissues. The signal of the bone is dominated by two T_2s of about 10 and 150 µs. Hence, during the imaging process, a relatively long dead time of 40 µs was chosen deliberately to suppress the shorter component that cannot be resolved to the targeted sub-millimeter resolution and to focus on the longer-T_2 contributions, as well as to increase the PSF-limited resolution (27).

In-vivo imaging of a knee and a head was conducted in healthy volunteers according to applicable ethics approval, and written informed consent was obtained from all subjects. For knee imaging, the dead time was intentionally increased to 200 μs to extend the inner k-space and thus reduce chemical shift artifacts.

An imaging phantom with a range of T_2 values was created by filling six solutions of $MnCl_2$ with concentrations of 240, 120, 60, 30, 15 and 7.5 mMol into glass vials. For measuring the transverse relaxation times, the solutions were filled into glass spheres of 20 mm diameter to minimize susceptibility effects. Free induction decay (FID) signals were acquired and fitted with single exponentials, providing decay constants of 54, 92, 181, 341, 663 and 1271 µs respectively. For T_2 mapping, a series of images was acquired with constant gap (k_{gap} = 47) and different dead times (Δt = 55, 100, 200, 400, 600 µs). The signal decay was fitted exponentially with the echo time chosen as $TE = \Delta t$.

2.5 Image reconstruction and processing

Images were reconstructed using an iterative conjugate gradient algorithm (36) complemented by sampling density calculation (37) and pulse correction for modulated pulses (38).

For determining the SNR in images, additional noise data was acquired in the absence of RF excitation. The average signal over a region of interest (ROI) in the magnitude sample image was divided by the standard deviation of the noise image in the same ROI. The SNR efficiency was obtained as $SNR_{eff} = SNR/\sqrt{scan\ time}$. Finally, the relative scan time for equal SNR was calculated according to

$$\tau_{scan} = \left(\frac{SNR_{eff}^{PETRA}}{SNR_{eff}^{HYFI}}\right)^2$$

When interpreting a series of images acquired at different dead time Δt, the echo time is defined as TE = Δt for both PETRA and HYFI.

2.6 Simulations

The k-space signal of spheres with 50, 30, 18 and 9 mm diameter and T_2s of 100 µs was created analytically (39) and images were reconstructed with the algorithm described above.

3 Results

The effect of the decay coefficient A on image quality and scan efficiency is illustrated with 3D simulations (Fig. 4). Corresponding image profiles are shown in Fig. S2. As the decay coefficient A increases, the relative number of excitation needed to fill the inner-k-space, n_{gap}, diminishes, increasing the scan efficiency. For this sample, images without noticeable artifacts are obtained with A < 0.1.

The phantom experiment in Fig. 5 demonstrates the HYFI principle over a large range of A. For A = 0, the inner k-space is acquired in an SPI fashion, leading there to a constant plateau of T_2 weighting, maximum n_{gap} and artifact-free images. When A increases, radial shells with restricted decay replace part of the SPI plateau and n_{gap} diminishes. However, this also creates progressively increasing irregularities in the MTF which in turn lead to increasingly large ringing artifacts out- and inside the imaged object.

In Fig. 6, the performance of PETRA and HYFI is compared for imaging a sample of bovine tibia. Both techniques lead to high quality images depicting fine trabecular bone structure. Other details appear in the maximum intensity projection, such as glue from the coil conductor and the fixation tape. In HYFI, the choice of a small A = 0.04 is sufficient to significantly improve the SNR efficiency compared to PETRA, which translates in a 25% decrease of total scan time for same SNR.

The head images with an unusually high bandwidth of 2 MHz presented in Fig. 7 confirm the above results. The SNR efficiency of HYFI is enhanced compared to PETRA and lead to 40% scan time reduction for same SNR while preserving image quality.

Figure 8 shows the influence of the dead time gap on chemical shift artifacts in ZTE knee imaging. At minimum dead time Δt = 5.5 µs leading to k_{gap}= 1.4 Nyquist dwells, signal intensity is maximized and moreover, the missing data points can be reconstructed algebraically leading to minimum scan duration. However, due to signal dephasing during the encoding duration of 480 µs, chemical shift artefacts appear at water-fat boundaries (17). Increasing the dead time to 200 µs, enlarges the inner k-space to 50 Nyquist dwells radius and thus reduces the acquisition time range for data located in this region. In PETRA (Fig. 8b), signal can dephase only within 1 Nyquist dwell = 4 µs. Hence, while accepting a loss of signal intensity associated to the longer dead time, chemical shift artifacts are strongly reduced and resolution at water-fat interfaces is improved. However, scan time is substantially increased. In the same circumstances, HYFI provides similar image quality but reduces the acquisition duration for same SNR by 62% as compared to PETRA (Fig. 8c).

T_2 mapping of short-T_2 samples is demonstrated in Fig. 9. To enable accurate fitting, the inner k-space was deliberately increased up to the outer limit of the support such that the whole k-space was acquired within a restricted time range. In this way, PETRA approaches pure SPI acquisition (24). Figure 9a shows that at TE = 55 µs all vials are well depicted and image intensity drops at larger TE in

the short-T_2 samples. For same image and T_2 map quality, the scan time of HYFI is 62% lower than PETRA. Figure 9b shows a good correspondence between the fit of average map intensities and the fit of the FID, especially in the short-T_2 range. However, two observations can be made: 1) There is an increasing divergence between FIDs and T_2 maps as T_2 gets larger, and 2) the relaxation times fitted from the HYFI data are slightly but consistently smaller than the PETRA results. The first observation is assigned to residual B0 inhomogeneity in the samples used for FID measurements, leading to smaller effective T_2* values. The second effect results from the definition of the echo time $TE = \Delta t$ which suits PETRA better than HYFI. In the radial shells of HYFI, data is acquired for a duration t_{acq} following Δt. During that time, the signal decays and appears smaller than in PETRA, therefore generating a reduction in image intensity that increases with TE and thus leads to smaller fitted T_2-values.

4 Discussion

HYFI, a new ZTE-based method with hybrid filling of the inner k-space was described and its performance in the presence of large k-space gaps was studied. It was demonstrated that with HYFI, substantial reductions in scan time can be enabled while preserving image quality as compared to the PETRA technique. The advantage of HYFI increases with gap size and is therefore of particular interest at high bandwidth, large minimum RF dead times, and large dead times selected to manipulate image contrast. The technique was successfully employed for imaging on different phantoms and in vivo.

Using HYFI with high efficiency and fidelity necessitates a suitable choice of the parameter pair (A, T_2). The simulations in Fig. 4 demonstrate that in the presence of a single T_2, $A \lesssim 0.1$ provides considerable savings in scan time at still high image quality. However as A is increased, artifacts become more likely due to coherent interaction of increasingly large PSF side lobes, occurring predominantly in the center of large objects.

In more common cases involving different tissues and molecules and thus a range of transverse relaxation times, the choice of the target T_2 requires extra considerations. Selecting the smallest T_2 present in the sample is safe but usually too conservative. Typically, components with $T_2 < \Delta t$ have little influence on the final image and choosing a target $T_2 = \Delta t$ can be considered an appropriate rule of thumb (Fig. 9). Moreover, the target T_2 might be increased to values larger than Δt without degrading image quality if the signal is dominated by components with longer T_2. In the presented in-vivo data, target T_2s of a few hundreds of microseconds still lead to images without noticeable artifacts (Figs. 7 and 8) although components with clearly faster relaxation but lower intensity, e.g. myelin or collagen, are present. Only if the latter signals should be extracted from the data, they need to be considered for setting the target T_2.

In the performed experiments, the reductions in scan time (for same SNR) of HYFI with respect to PETRA range from 25% to 62% (Figs. 6-8). The influencing factors are gap size, spatial resolution, and the parameter pair (A, T_2). The relative number of excitations required to fill the inner k-space with HYFI decreases with increasing gap size when compared to PETRA (Fig. 2). This explains why the best HYFI performance is obtained in Figs. 8 and 9, were gaps were deliberately increased to high values to reduce chemical shift artefacts and perform T_2 mapping, respectively. The resolution determines the time spent for the acquisition of the outer k-space which in turn affects the relative scan time spent on the inner k-space. Thus, as resolution and hence scan time are increased, the absolute time difference between PETRA and HYFI does not change but the relative advantage of HYFI diminishes. Finally, the selection of the parameter pair (A, T_2) influences the k-space trajectory and affects both scan time and image SNR. As A increases, the SPI region decreases and is replaced by radial acquisitions which lead to higher k-space data density and thus a reduction of image noise variance (27). However, the data points experience stronger T_2 weighting which translates into a smaller integral of the MTF (Fig. 1) and hence to a smaller PSF main lobe (Fig. 2), leading to decreased voxel intensity. These two effects partly compensate each other. For small decay coefficients they even largely balance and the improvement of HYFI in SNR efficiency can be well approximated as if arising from scan time reduction alone. High-resolution imaging of short-T_2 components benefits from the use of high gradients (40). As shown in Fig. 6, bone tissue with $T_2 \approx$ 150 µs can be imaged at an isotropic resolution of 400 µm using a gradient strength of 200 mT/m. Such high gradients induce high bandwidths and thus large k-space gaps, especially in large field of views as required for imaging in humans (Fig. 7). In such circumstances, substituting a large part of the SPI region by radial spokes with HYFI particularly improves scanning efficiency. Moreover, at large gradient amplitude Cartesian SPI acquisition can produce significant mechanical vibrations and acoustic noise due to partly large gradient switching between k-space directions. With HYFI, as long as the gradient can be used at full duty cycle (i.e. without switching back to zero), these effects are significantly reduced since k-space directions are uniformly distributed in all directions and sequentially accessed along a spiral trajectory (41) requiring slower gradient switching, thus clearly improving patient comfort.

The results of this work indicate the potential of HYFI for direct imaging of ultra-short-T_2 components such as in the myelin bilayer in the brain. However as observable in Fig. 7, basic ZTE sequences lead to mostly proton density-weighted images and some kind of selectivity is required to isolate the tissues of interest. One possibility to achieve T_2 selection uses post-processing of a series of images acquired after different dead times. An example of such an experiment is shown in Fig. 9, where T_2 mapping of $MnCl_2$ solutions was performed by fitting exponential signal decays. This kind of approach has been shown to enable T_2 selection of ultra-fast relaxing MR signals in the brain which can potentially be assigned to the myelin bilayer (10). Further improvements in quantification with HYFI-based T_2

mapping are expected with a more advanced definition of TE or signal models taking into account the precise sequence timing.

Clinical scanners with state-of-the-art hardware specifications (e.g. RF switching time $\sim 30\ \mu s$ (42), gradient slew rate $\sim$200 mT/m, and maximum gradient strength $\sim$80 mT/m, yet at limited duty cycle (17)) may be used for short-T_2 PETRA imaging and will lead to gap sizes of about 30-40 Nyquist dwells. Thus, assuming a TR of a few milliseconds, the acquisition of the inner k-space takes several minutes (c.f. Fig. 2). In such a situation and as illustrated in this paper, substantial improvement in SNR efficiency can be expected when using HYFI instead of PETRA. If the same scanners are used with lower bandwidth (e.g. G < 40 mT/m), the advantage of HYFI is limited to lower acoustic noise and reduced mechanical vibrations. In the special case of a combination of low gradients and large dead times (e.g. G = 10 mT/m, RF switching time $\sim 50\ \mu s$), the dead time could be used to ramp up the gradient to its target strength, thus allowing smaller excitation bandwidths at reduced gap sizes and avoiding the need of HYFI, yet at the price of reduced spatial resolution (27). A similar idea was exposed in the ramped hybrid encoding (RHE) technique (43), where the readout gradient is lowered during RF excitation and increased to full strength afterwards during data acquisition. In such cases, k-space calibration is required since timing errors and eddy current effects distort the k-space trajectory. Other alternatives to PETRA and hence HYFI are SWIFT (44) and cSWIFT (45), where gaps are very small or inexistent, respectively. However, the first one comes at an SNR penalty and limited bandwidth (46) and the second approach is particularly sensitive to RF coil loading variations.

Finally, there are situations where a large part of the data should be acquired within a small time range as required for chemical shift artifact reduction or T_2 mapping. For example, for performing the latter, longer dead times should be used to include the complete k-space in the gap as performed in Fig. 9, leading to a pure SPI acquisition with spherical support in the PETRA case. Note that in this context, gradients should be switched on *before* the RF pulse since large gaps are actually targeted. Hence, even with clinical scanners, HYFI can be considered as an efficient alternative for SPI methods (24,47).

5 Conclusion

The HYFI technique provides both high SNR efficiency and image quality, thus outperforming previously known ZTE-based pulse sequences. It is particularly advantageous in situations involving large dead times or high gradient strengths where PETRA suffers from long and noisy SPI acquisitions. Promising applications include direct imaging of ultra-short T_2 components, such as e.g. the myelin bilayer or collagen, T_2 mapping of ultra-fast relaxing signals, and ZTE imaging with reduced chemical shift artifacts.

References

(1) Cao H, Nazarian A, Ackerman JL, Snyder BD, Rosenberg AE, Nazarian RM, Hrovat MI, Dai G, Mintzopoulos D, Wu Y. Quantitative 31P NMR spectroscopy and 1H MRI measurements of bone mineral and matrix density differentiate metabolic bone diseases in rat models. Bone 2010;46:1582–90.

(2) Du J, Bydder GM. Qualitative and quantitative ultrashort-TE MRI of cortical bone. NMR Biomed 2013;26:489–506.

(3) Wehrli FW. Magnetic resonance of calcified tissues. J Magn Reson 2013;229:35–48.

(4) Peto S, Gillis P, Henri VP. Structure and dynamics of water in tendon from NMR relaxation measurements. Biophys J 1990;57:71–84.

(5) Robson MD, Benjamin M, Gishen P, Bydder GM. Magnetic resonance imaging of the Achilles tendon using ultrashort TE (UTE) pulse sequences. Clin Radiol 2004;59:727–35.

(6) Rahmer J, Börnert P, Groen J, Bos C. Three-dimensional radial ultrashort echo-time imaging with T2 adapted sampling. Magn Reson Med 2006;55:1075–82.

(7) Nayak KS, Pauly JM, Gold GE, Nishimura DG. Imaging ultra-short T2 species in the brain. Proc, ISMRM, 8th Annu Meet Denver 2000:509.

(8) Du J, Ma G, Li S, Carl M, Szeverenyi NM, VandenBerg S, Corey-Bloom J, Bydder GM. Ultrashort echo time (UTE) magnetic resonance imaging of the short T2 components in white matter of the brain using a clinical 3T scanner. Neuroimage 2014;87:32–41.

(9) Wilhelm MJ, Ong HH, Wehrli SL, Li C, Tsai PH, Hackney DB, Wehrli FW. Direct magnetic resonance detection of myelin and prospects for quantitative imaging of myelin density. Proc Natl Acad Sci U S A 2012;109:9605–10.

(10) Weiger M, Froidevaux R, Baadsvik EL, Brunner DO, Rösler MB, Pruessmann KP. Advances in MRI of the myelin bilayer. Neuroimage 2020;217.

(11) Bergin CJ, Pauly JM, Macovski A. Lung parenchyma: Projection reconstruction MR imaging. Radiology 1991;179:777–81.

(12) Kuethe DO, Adolphi NL, Fukushima E. Short data-acquisition times improve projection images of lung tissue. Magn Reson Med 2007;57:1058–64.

(13) Gibiino F, Sacolick L, Menini A, Landini L, Wiesinger F. Free-breathing, zero-TE MR lung imaging. Magn Reson Mater Physics, Biol Med 2015;28:207–15.

(14) Gruwel MLH, Latta P, Tanasiewicz M, Volotovskyy V, Šramek M, Tomanek B. MR imaging of teeth using a silent single point imaging technique. Appl Phys A Mater Sci Process 2007;88:763–7.

(15) Hövener JB, Zwick S, Leupold J, Eisenbei AK, Scheifele C, Schellenberger F, Hennig J, Elverfeldt D V., Ludwig U. Dental MRI: Imaging of soft and solid components without ionizing radiation. J Magn Reson Imaging 2012;36:841–6.

(16) Weiger M, Pruessmann KP, Bracher AK, Köhler S, Lehmann V, Wolfram U, Hennel F, Rasche V. High-resolution ZTE imaging of human teeth. NMR Biomed 2012;25:1144–51.

(17) Weiger M, Pruessmann KP. Short-T2 MRI: Principles and recent advances. Prog Nucl Magn Reson Spectrosc 2019;115:237–70.

(18) Hafner S. Fast imaging in liquid and solids with the back-projection low angle shot (blast) technique. Magn Reson Imaging 1994;12:1047–51.

(19) Wu Y, Dai G, Ackerman JL, Hrovat MI, Glimcher MJ, Snyder BD, Nazarian A, Chesler D a. Water- and fat-suppressed proton projection MRI (WASPI) of rat femur bone. Magn Reson Med 2007;57:554–67.

(20) Weiger M, Pruessmann KP. MRI with zero echo time. Encycl Magn Reson 2012;1:311–22.

(21) Grodzki DM, Jakob PM, Heismann B. Ultrashort echo time imaging using pointwise encoding time reduction with radial acquisition (PETRA). Magn Reson Med 2012;67:510–8.

(22) Kuethe DO, Caprihan a, Lowe IJ, Madio DP, Gach HM. Transforming NMR data despite missing points. J Magn Reson 1999;139:18–25.

(23) Emid S. Ultra high resolution multiple quantum spectroscopy in solids. Physica 1985;128B:79–80.

(24) Balcom BJ, Macgregor RP, Beyea SD, Green DP, Armstrong RL, Bremner TW. Single-point ramped imaging with T1 enhancement (SPRITE). J Magn Reson 1996;123:131–4.

(25) Weiger M, Brunner DO, Tabbert M, Pavan M, Schmid T, Pruessmann KP. Exploring the bandwidth limits of ZTE imaging: Spatial response, out-of-band signals, and noise propagation. Magn Reson Med 2015;74:1236–47.

(26) Froidevaux R, Weiger M, Brunner DO, Dietrich BE, Wilm BJ, Pruessmann KP. Filling the dead-time gap in zero echo time MRI: Principles compared. Magn Reson Med 2018;79:2036–45.

(27) Froidevaux R, Weiger M, Rösler MB, Brunner DO, Dietrich BE, Reber J, Pruessmann KP. High-resolution short-T2 MRI using a high-performance gradient. Magn Reson Med 2020;00:11–4.

(28) Froidevaux R, Weiger M, Rösler MB, Brunner DO, Pruessmann KP. HYFI: Hybrid filling of the dead-time gap for faster zero echo time imaging. Proc 27th Annu Meet ISMRM, Montr Canada 2019:943.

(29) Froidevaux R, Weiger M. Magnetic resonance imaging method with hybrid filling of k-space. WIPO, Patent WO 2019/072778 A1, 2019.

(30) Brunner DO, Furrer L, Weiger M, Baumberger W, Schmid T, Reber J, Dietrich BE, Wilm BJ, Froidevaux R, Pruessmann KP. Symmetrically biased T/R switches for NMR and MRI with microsecond dead time. J Magn Reson 2016;263:147–55.

(31) Dietrich BE, Brunner DO, Wilm BJ, BarmeT C, Gross S, Kasper L, Haeberlin M, Schmid T, Vannesjo SJ, Pruessmann KP. A field camera for MR sequence monitoring and system analysis. Magn Reson Med 2016;75:1831–40.

(32) Weiger M, Overweg J, Rösler MB, Froidevaux R, Hennel F, Wilm BJ, Penn A, Sturzenegger U, Schuth W, Mathlener M, et al. A high-performance gradient insert for rapid and short-T 2 imaging at full duty cycle. Magn Reson Med 2018;79:3256–66.

(33) Froidevaux R, Weiger M, Rösler MB, Brunner DO, Dietrich BE, Reber J, Pruessmann KP. Pushing the limits of short-T2 MRI: 200 mT/m gradient strength and 2 MHz bandwidth. Proc 27th Annu Meet ISMRM, Paris 2018:0534.

(34) Weiger M, Brunner DO, Schmid T, Froidevaux R, Rösler MB, Gross S, Pruessmann KP. A virtually 1H-free birdcage coil for zero echo time MRI without background signal. Magn Reson Med 2017;78:399–407.

(35) Rösler MB, Weiger M, Brunner DO, Schmid T, Pruessmann KP. An RF birdcage coil designed for an insert gradient coil dedicated to short-T2 MRI. Proc 26th Annu Meet ISMRM, Honolulu 2017:2668.

(36) Pruessmann KP, Weiger M, Börnert P, Boesiger P. Advances in sensitivity encoding with arbitrary k-space trajectories. Magn Reson Med 2001;46:638–51.

(37) Zwart NR, Johnson KO, Pipe JG. Efficient sample density estimation by combining gridding and an optimized kernel. Magn Reson Med 2012;67:701–10.

(38) Li C, Magland JF, Seifert AC, Wehrli FW. Correction of excitation profile in zero echo time (ZTE) imaging using quadratic phase-modulated RF pulse excitation and iterative reconstruction. IEEE Trans Med Imaging 2014;33:961–9.

(39) Cheng GK, Sarlls JE, Özarslan E. Three-dimensional analytical magnetic resonance imaging phantom in the Fourier domain. Magn Reson Med 2007;58:430–6.

(40) Froidevaux R, Weiger M, Rösler MB, Wilm B, Hennel F, Luechinger R, Dietrich BE, Reber J, Pruessmann KP. Ultra-high-bandwidth , high-resolution MRI of fast relaxing spins. Proc 26th Annu Meet ISMRM, Honolulu 2017:4037.

(41) Wong STS, Roos MS. A strategy for sampling on a sphere applied to 3D selective RF pulse design. Magn Reson Med 1994;32:778–84.

(42) Wiesinger F, Sacolick LI, Menini A, Kaushik SS, Ahn S, Veit-haibach P, Delso G, Shanbhag DD. Zero TE MR Bone Imaging in the Head 2015;75:107–14.

(43) Jang H, Wiens CN, McMillan AB. Ramped hybrid encoding for improved ultrashort echo time imaging. Magn Reson Med 2016;76:814–25.

(44) Garwood M, Idiyatullin D, Corum CA, Chamberlain R, Moeller S, Kobayashi N, Lehto LJ, Zhang J, O'Connell R, Tesch M, et al. Capturing Signals from Fast-relaxing Spins with Frequency-Swept MRI: SWIFT. Encycl Magn Reson 2012;1:367–80.

(45) Idiyatullin D, Suddarth S, Corum CA, Adriany G, Garwood M. Continuous SWIFT. J Magn Reson 2012;220:26–31.

(46) Weiger M, Pruessmann KP, Hennel F. MRI with zero echo time: Hard versus sweep pulse excitation. Magn Reson Med 2011;66:379–89.

(47) Kaffanke JB, Romanzetti S, Dierkes T, Leach MO, Balcom BJ, Shah NJ. Multi-Frame SPRITE: A method for resolution enhancement of multiple-point SPRITE data. J Magn Reson 2013;230:111–6.

Figure Captions

Figure 1: ZTE data acquisition. a) The gradient G applied for radial center-out encoding is ramped up before RF excitation. The initial part of the signal cannot be acquired due to the dead time Δt (white dots). b) After each excitation, a different radial spoke is acquired to fill a 3D k-space volume. The dead time leads to a spherical gap of radius k_{gap}. c-e) PETRA, WASPI, and HYFI provide the data missing in the gap in different ways. Left: 1D depiction of T_2 – related MTF in k-space. Right: 2D depiction of inner k-space acquisition geometry. c) In PETRA, the inner k-space is acquired single-point-wise in a Cartesian fashion leading to constant T_2 weighting. d) In WASPI, a second set of radial acquisitions is performed at lower gradient strength, giving rise to increased and potentially strong T_2 weighting. e) HYFI consists of a Cartesian core ($k < k_{SPI}$) surrounded by several shells with radial acquisition ($k > k_{SPI}$). In this way, the T_2 decay is restricted to a given range R, wherein R is chosen such as to allow shorter scan time with minimum loss of image quality. Note that the figure partially reuses schemes of previous publications of the same author (26,27).

Figure 2: Influence of the decay coefficient A on scan time and depiction fidelity. a) Number of excitations required to fill the SPI core (N_{SPI}) as a function of the decay coefficient A for different ratios $\Delta t/T_2$ and gap sizes k_{gap}. For given gap and $\Delta t/T_2$ ratio, as A increases, N_{SPI} stays constant up to a particular value A_0 (Equ. 4) and then starts diminishing. In more detail, when A is small, the complete inner k-space must be acquired single-point-wise since $k_{SPI} > k_{gap}$ and hence $N_{SPI} = \frac{4}{3}\pi\, k_{gap}^3$. However, for larger A, when $k_{SPI} \leq k_{gap}$, part of the inner k-space can be acquired radially. Hence the SPI core is limited to the sphere of radius k_{SPI} and $N_{SPI} = \frac{4}{3}\pi\, k_{SPI}^3$. In summary, this figure shows that for common situations where Δt is smaller or comparable to T_2, the volume of data that needs to be acquired in a time-consuming SPI manner rapidly decreases to almost negligible values even with relatively small decay coefficient. Assuming a TR of 1 ms this allows reducing scan time by several minutes compared to PETRA. b) Point spread function lineshapes. Calculations were done assuming T_2 = 100 Nyquist dwells and k_{gap} = *30*. As A increases from 0 (PETRA) to 1 (WASPI), the main lobe amplitude decreases and side lobes build up. Importantly, the PSF lineshapes are well preserved for $A \approx 0.1$ at which N_{SPI} is substantially decreased. Hence, HYFI is expected to reduce scan time while preserving image quality. More details PSFs are shown in Fig. S1. Note that PETRA and WASPI acquisitions are also obtained with values of A slightly larger 0 and smaller than 1 respectively (c.f. Matlab script for more details).

Figure 3: Number of excitations required to fill the complete inner k-space by the different techniques. A decay with T_2 = 100 Nyquist dwells is assumed. Circles at the top illustrate the acquisition geometries. The number of excitations, N_{gap}, required to fill the inner 3D k-space evolves with k_{gap}^3 for PETRA and k_{gap}^2 for WASPI. In the proposed HYFI method, inner k-space is filled by a combination of SPI and radial acquisitions, and thus the green area enclosed by the curves for PETRA

and WASPI becomes accessible. Green lines represent selected HYFI acquisitions with decay coefficients A = 0.1 and 0.5.

Figure 4: 3D HYFI simulations illustrating the effect of the amplitude coefficient A on image quality and scan efficiency. Imaging of spheres with 50, 30, 18 and 9 mm diameter was simulated assuming T_2 = 100 µs and k_{gap} = 30 Nyquist dwells. Other parameters are listed in Table 1.

As A increases, k_{SPI} decreases and the relative number of excitations needed to acquire the inner k-space, n_{gap}, decreases. It quickly reaches 28% (A = 0.06) with preserved image quality. Above this value, n_{gap} decreases slower and artifacts start to appear in the center of the larger spheres, suggesting that for such samples the optimal decay coefficient A resides below 0.1. Image profiles of a few representative cases are shown in Fig. S2.

Figure 5: Demonstration of HYFI principle in a phantom experiment. The first row represents the decay coefficient A growing from 0 to 1. Below are the corresponding 1D k-space T_2–related MTFs and the relative number of excitations required to fill the gap, n_{gap}. The resulting images are shown in the two bottom rows with linear and logarithmic greyscales.

Figure 6: Bone imaging. a) Picture of the imaged segment of a bovine tibia (Here will be a statement saying that this picture is reproduced from ref 27 as soon the permission is received from Wiley). b) Comparison of PETRA and HYFI, with the decay coefficient A, the total scan time T_{scan} in min:sec and the relative total scan time for same SNR, τ_{scan} (including both inner and outer k-space). c) Maximum intensity projection of the HYFI image demonstrating high image quality over the whole field of view. The glue fixing the copper coil to the glass support and the tape holding the sample to the bed are also depicted.

Figure 7: High gradient head imaging. The displayed parameters are the decay coefficient A, the total scan time T_{scan} in min:sec and the relative scan time for same SNR, τ_{scan}. Top row: Three perpendicular slices of the same 3D volume acquired with PETRA. Bottom row: The corresponding HYFI images acquired with considerably reduced τ_{scan}.

Figure 8: Knee imaging. a) Algebraic ZTE imaging with short dead time and hence small gap, short scan time, but relatively strong chemical shift artefacts at water-fat boundaries as indicated by the red arrow. b) PETRA image with gap intentionally increased to 50 Nyquist dwells to acquire most of the data within a reduced time range and hence decrease chemical-shift artefacts c) Same as in b) except that the inner k-space is filled with HYFI (A = 0.1). In this case the relative scan time for same SNR (τ_{scan}) decreases by 62% while image quality is preserved.

Figure 9: Short-T_2 mapping in $MnCl_2$ solutions. a) Series of PETRA and HYFI images taken at different echo time $TE = \Delta t$ = 55, 100, 200, 400, 600 µs (only a subset is displayed). The maps of the transverse relaxation times were obtained by pixel-wise fitting the signal decay (last column). The scan time of individual images is given in min:sec (green) which shows a considerable reduction for

HYFI. b) The relative intensities of the signal averaged over each sample are plotted as a function of TE (circles and crosses) and overlaid with the free induction decay (FID) measured in each $MnCl_2$ solution (solid line). Fitted single-exponential T_2 values are given in the legend.

Tables

Sample	T_2	BW [kHz]	FOV [mm]	G [mT/m]	Δr [mm]	M	Δt [us]	k_{gap} [dw]	TR [ms]	NSA	Pulse	Pul. dur [us]	Coil	B0 [T]
Sphere simulations	100	1000	200	117.4	1	200	30	30	x	x	x	x	x	x
Stack of erasers	100	250	240	24.5	1.9	128	100.0	25	1	1	Block	2	Birdcage	7
Bone	200	766	90	199.9	0.4	256	40.0	31	1	8	Block	2	Surface	3
Head	200	2000	300	156.60	1.7	176	15.0	30	0.65	19	HSN	8	Birdcage	3
Knee	500	250	240	24.50	1.0	240	5.5	2	1	1	Block	2	Birdcage	7
Knee	500	250	240	24.50	1.0	240	200.0	50	1	1	Block	2	Birdcage	7
$MnCl_2$ vials	55	851.52	100	199.90	1.0	100	55.0	47	1	1	HSN	10	Surface	3
$MnCl_2$ vials	100	470	100	110.38	1.0	100	100.0	47	1	1	HSN	10	Surface	3
$MnCl_2$ vials	200	235	100	55.20	1.0	100	200.0	47	1	1	HSN	10	Surface	3
$MnCl_2$ vials	400	117.5	100	27.60	1.0	100	400.0	47	1	1	HSN	10	Surface	3
$MnCl_2$ vials	600	78	100	18.32	1.0	100	600.0	47	1	1	HSN	10	Surface	3

Table 1: Parameter table. The most important scan parameters are the target T_2, the bandwidth BW, the field of view FOV, the gradient G, the voxel size Δr, the matrix size M, the dead time Δt, the k-space gap k_{gap}, the repetition time TR, the number of sample averages NSA, the pulse type, the pulse duration, the coil type and the scanner field strength.

Supporting Information captions

Figure S1: 1D point spread functions (PSFs) for varying decay coefficients A. Simulations were performed for a matrix size of 200 pixels with T_2 = 100 Nyquist dwells, k_{gap} = 30 Nyquist dwells. For small values of A, the PSFs are very similar. However, the size of the side lobe quickly increases as A approaches 1.

Figure S2: Profiles of the 3D simulations illustrated in Fig. 4 demonstrating the effects of the decay coefficient A on image quality. Each profile is taken horizontally on the middle line of 4 selected images (A = 0, 0.04, 0.1, 0.2). As A increases, the overall image intensity decreases (by a factor smaller than A) and artifacts start to appear in the center of each object, especially in the largest one. Noticeably, the sharpness of the edges is hardly affected. All of these effects can be understood by looking at the HYFI MTF (Fig. 1e). First, as long as the overall PSF shape remains close to a delta function, the image intensity is related to the PSF maximum and hence to the integral of the MTF. As A increases, the MTF decreases by a factor A only in the inner k-space at the end of each radial shell. Thus, its integral and hence the image intensity decreases, but by a factor smaller than A. Second, the irregularities in the MTF arise around the k-space center and not on the edges of the k-space support (as opposed to usual Gibbs ringing). Hence, the related artifacts are expressed as low frequency modulation appearing essentially at the center of the larger objects where PSFs of surrounding pixels can constructively interfere. However, the high-frequency part of the object and hence the resolution of the edges remain mostly unchanged.

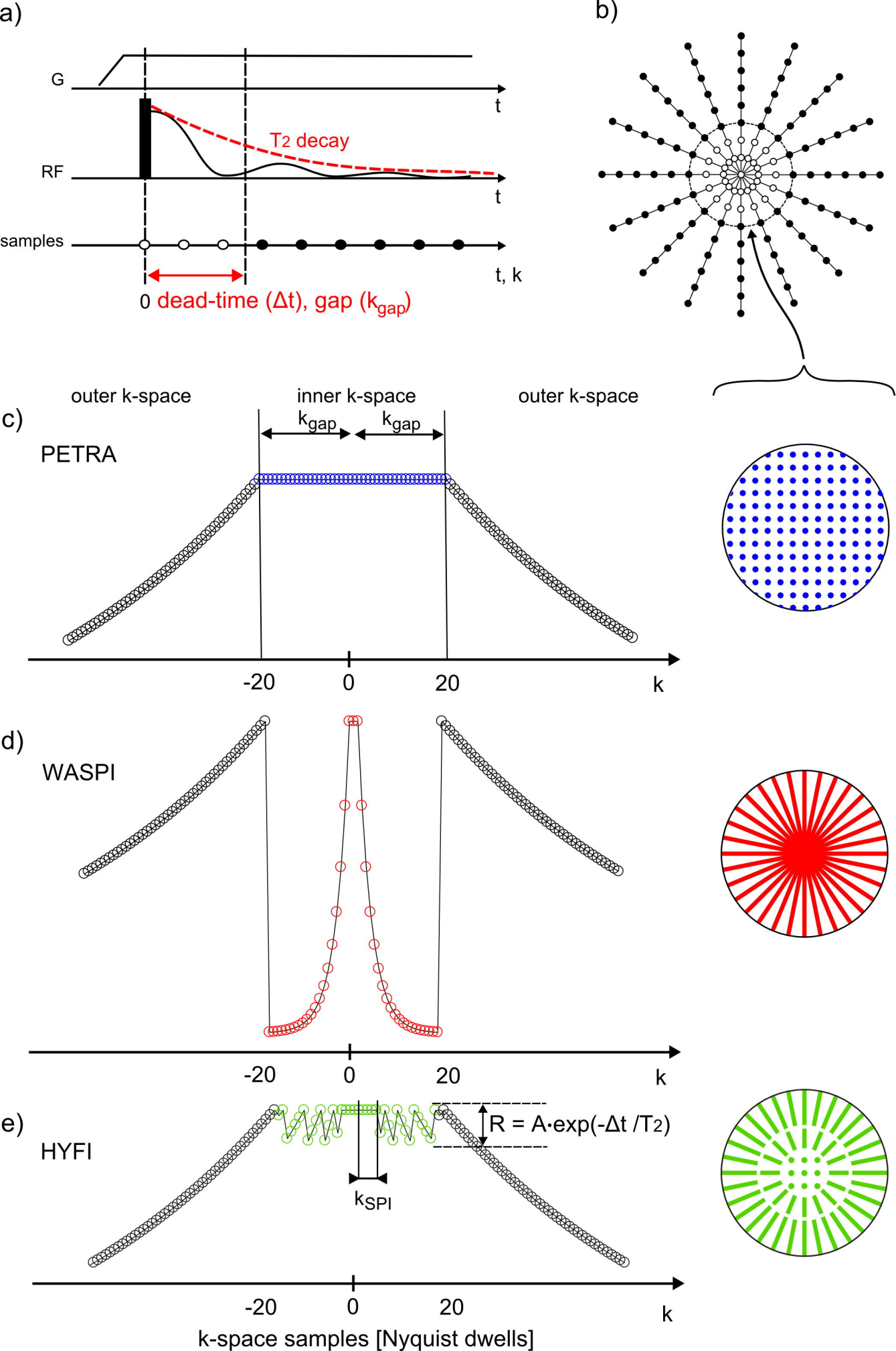
a)
G
t
T2 decay
RF
t
samples
t, k
0 dead-time (Δt), gap (kgap)
b)
outer k-space
inner k-space
outer k-space
c)
PETRA
kgap
kgap
-20
0
20
k
d)
WASPI
-20
0
20
k
e)
HYFI
R = A·exp(-Δt /T2)
kSPI
-20
0
20
k
k-space samples [Nyquist dwells]

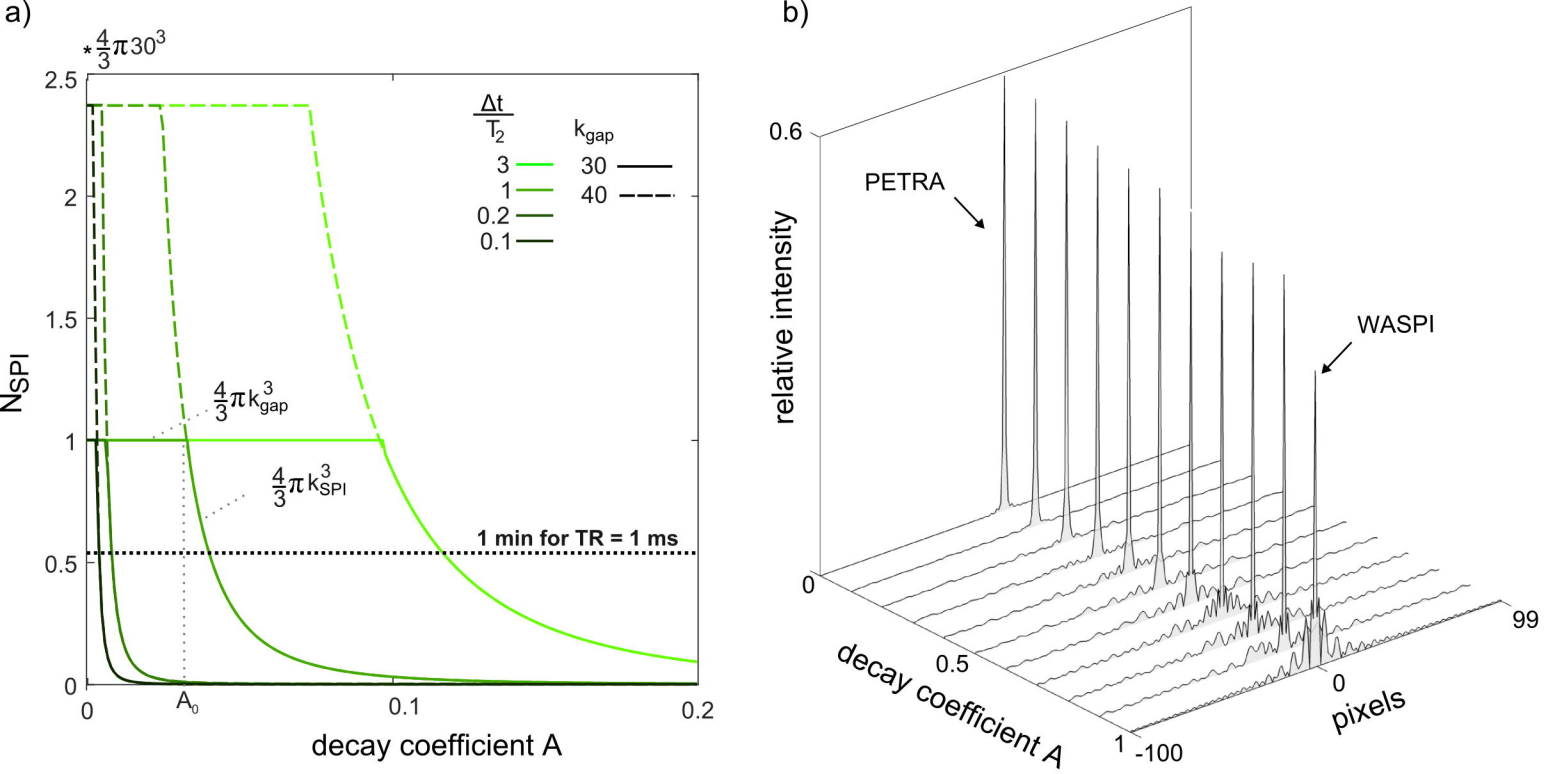
a)
$*\frac{4}{3}\pi 30^3$
$\frac{\Delta t}{T_2}$
3
1
0.2
0.1
k_{gap}
30
40
N_{SPI}
$\frac{4}{3}\pi k_{gap}^3$
$\frac{4}{3}\pi k_{SPI}^3$
1 min for TR = 1 ms
A_0
decay coefficient A
b)
PETRA
WASPI
relative intensity
decay coefficient A
pixels
0.6
0
0.5
1
-100
0
99

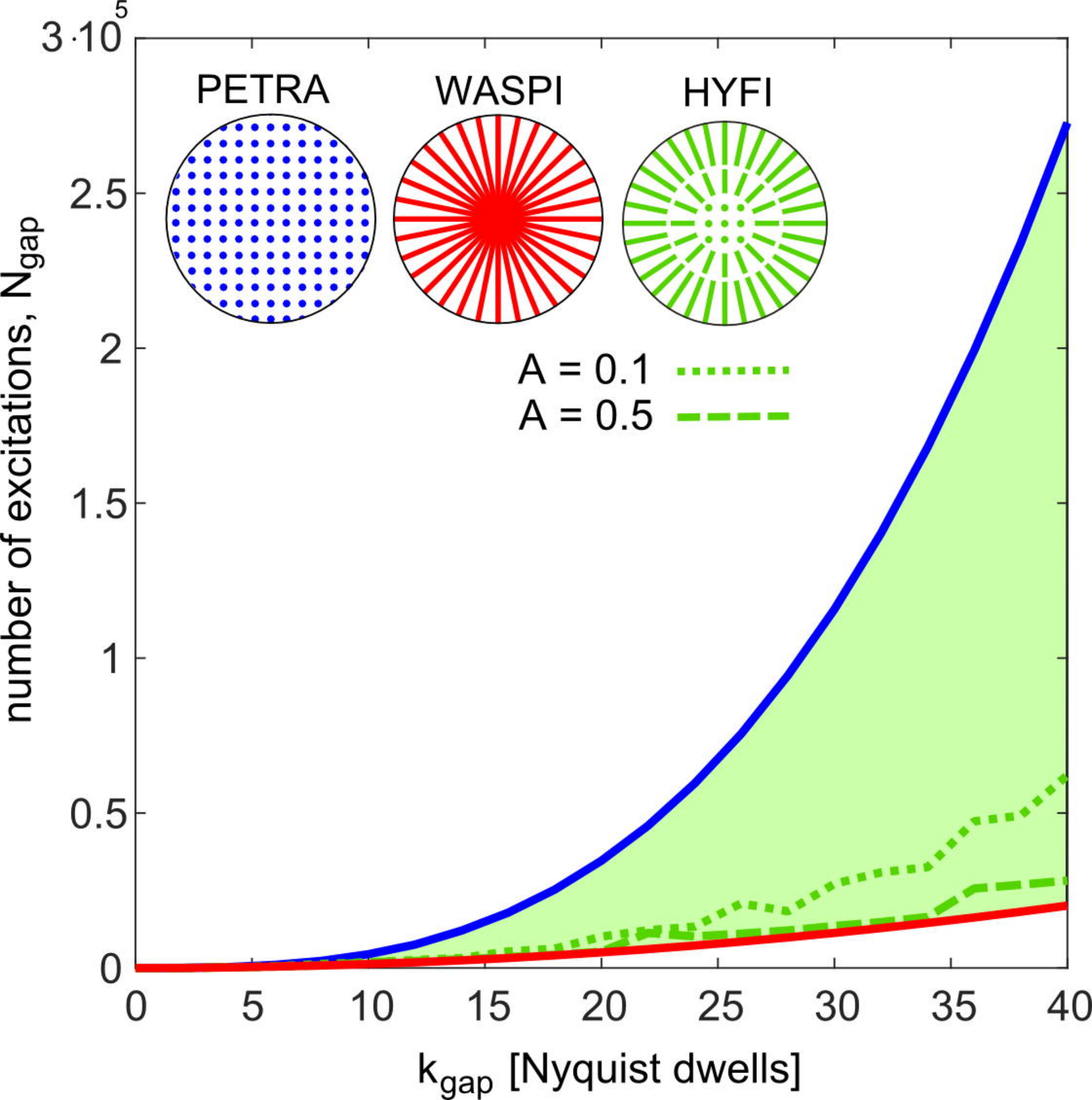
3·10^5
2.5
2
1.5
1
0.5
0
number of excitations, N_gap
PETRA
WASPI
HYFI
A = 0.1
A = 0.5
0
5
10
15
20
25
30
35
40
k_gap [Nyquist dwells]

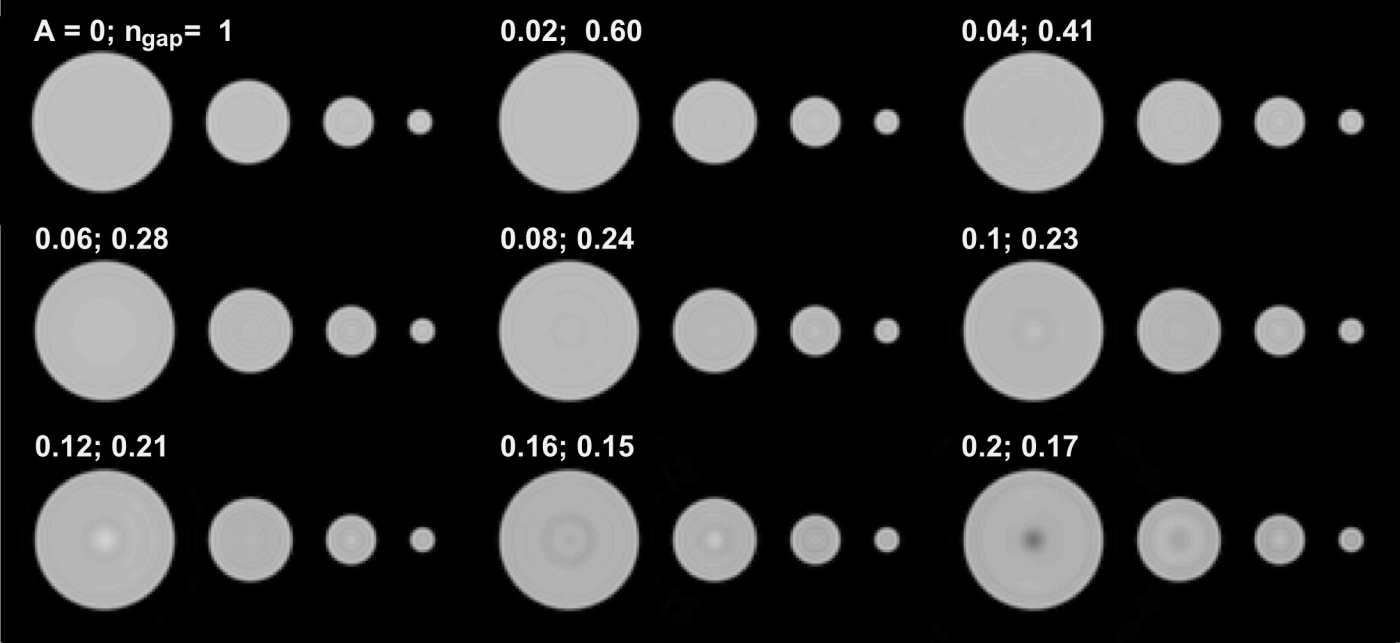
A = 0; n_gap= 1
0.02; 0.60
0.04; 0.41
0.06; 0.28
0.08; 0.24
0.1; 0.23
0.12; 0.21
0.16; 0.15
0.2; 0.17

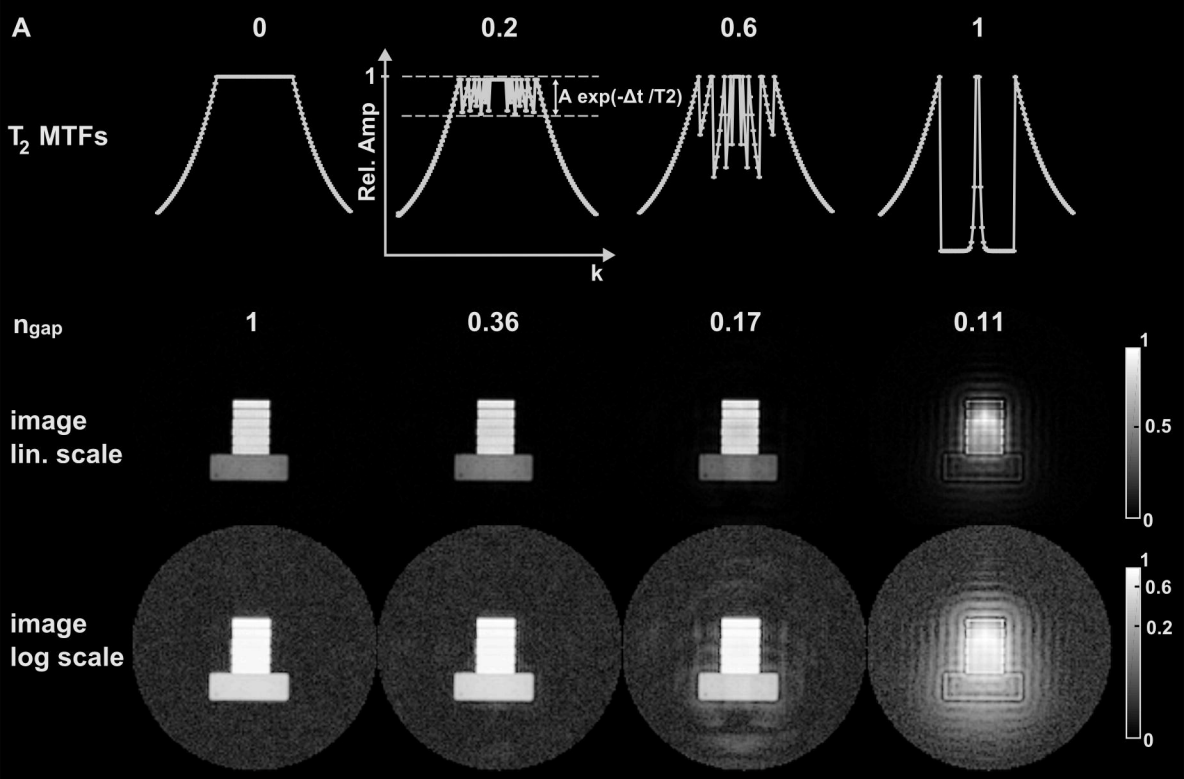
A
0
0.2
0.6
1
T2 MTFs
1
Rel. Amp
A exp(-Δt /T2)
k
ngap
1
0.36
0.17
0.11
image
lin. scale
1
0.5
0
image
log scale
1
0.6
0.2
0

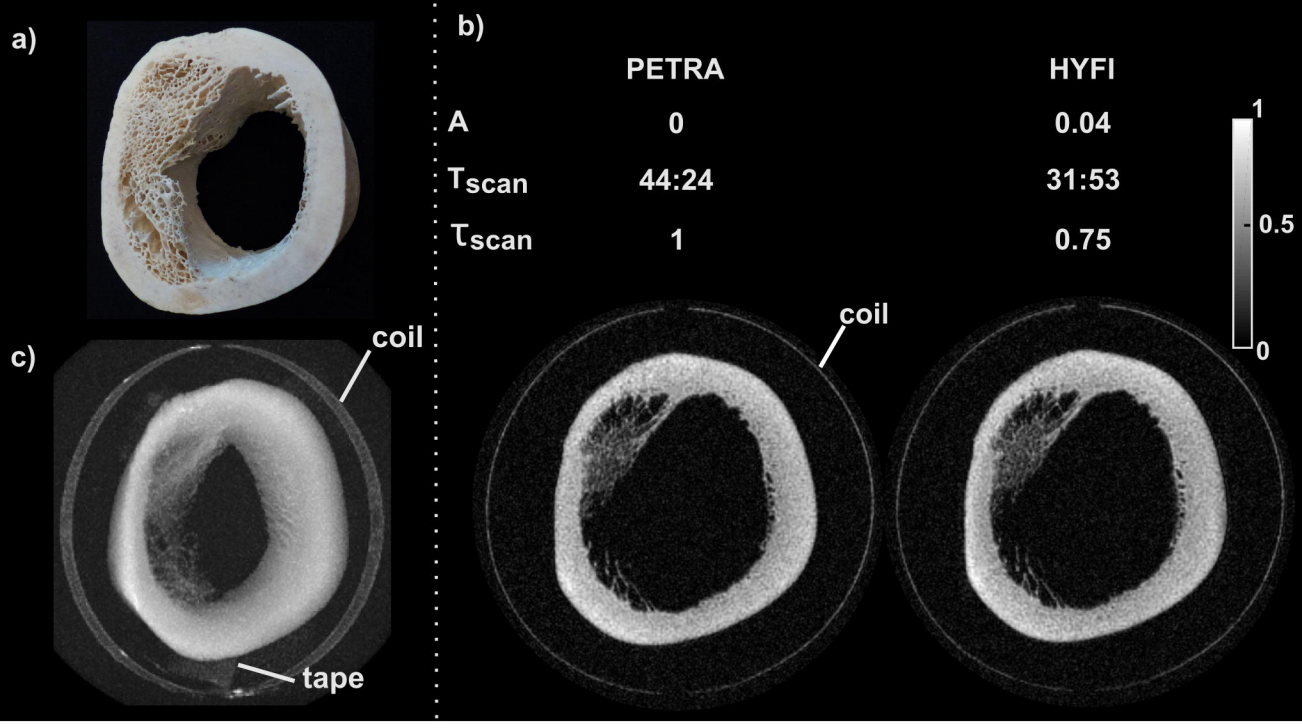
a)
b)
PETRA
HYFI
A
0
0.04
T_{scan}
44:24
31:53
τ_{scan}
1
0.75
1
0.5
0
c)
coil
tape
coil

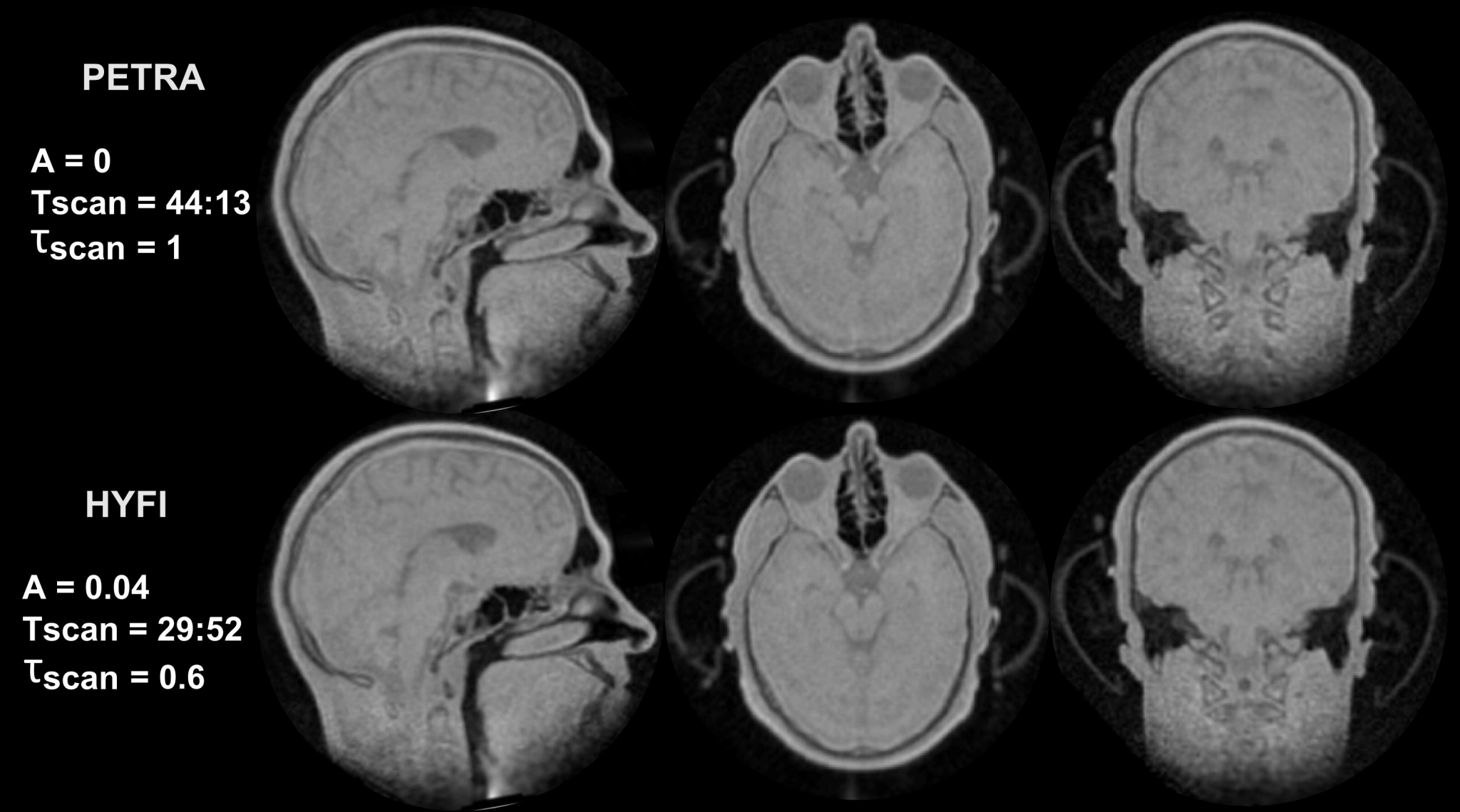
PETRA
A = 0
Tscan = 44:13
τscan = 1
HYFI
A = 0.04
Tscan = 29:52
τscan = 0.6

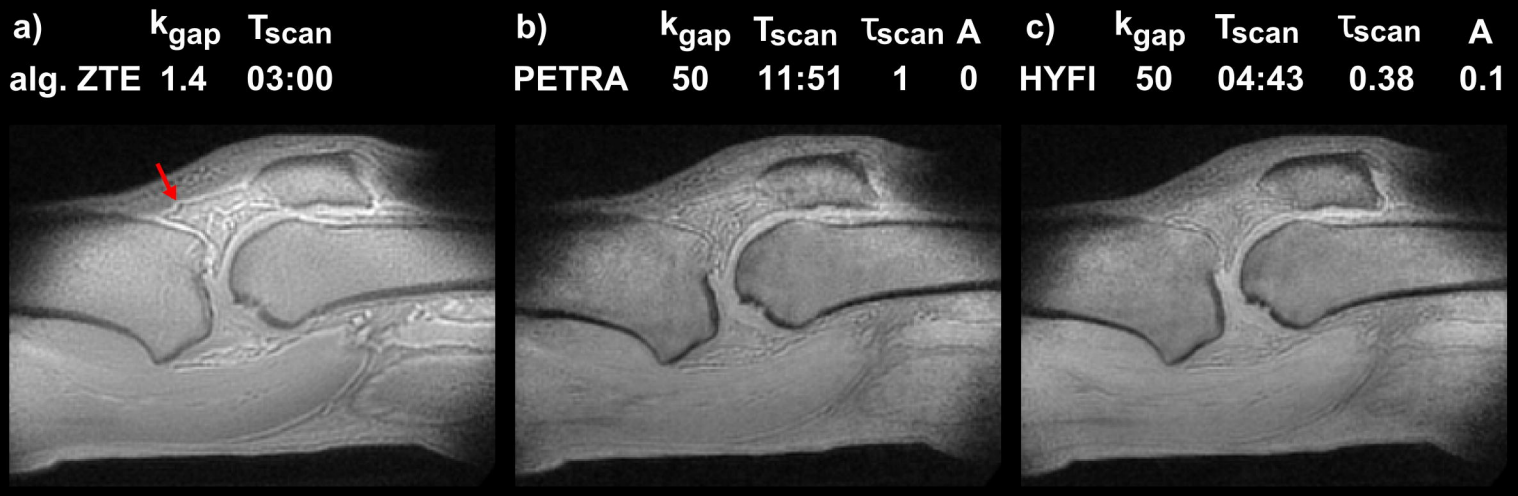
a) k_{gap} T_{scan}
alg. ZTE 1.4 03:00
b) k_{gap} T_{scan} τ_{scan} A
PETRA 50 11:51 1 0
c) k_{gap} T_{scan} τ_{scan} A
HYFI 50 04:43 0.38 0.1

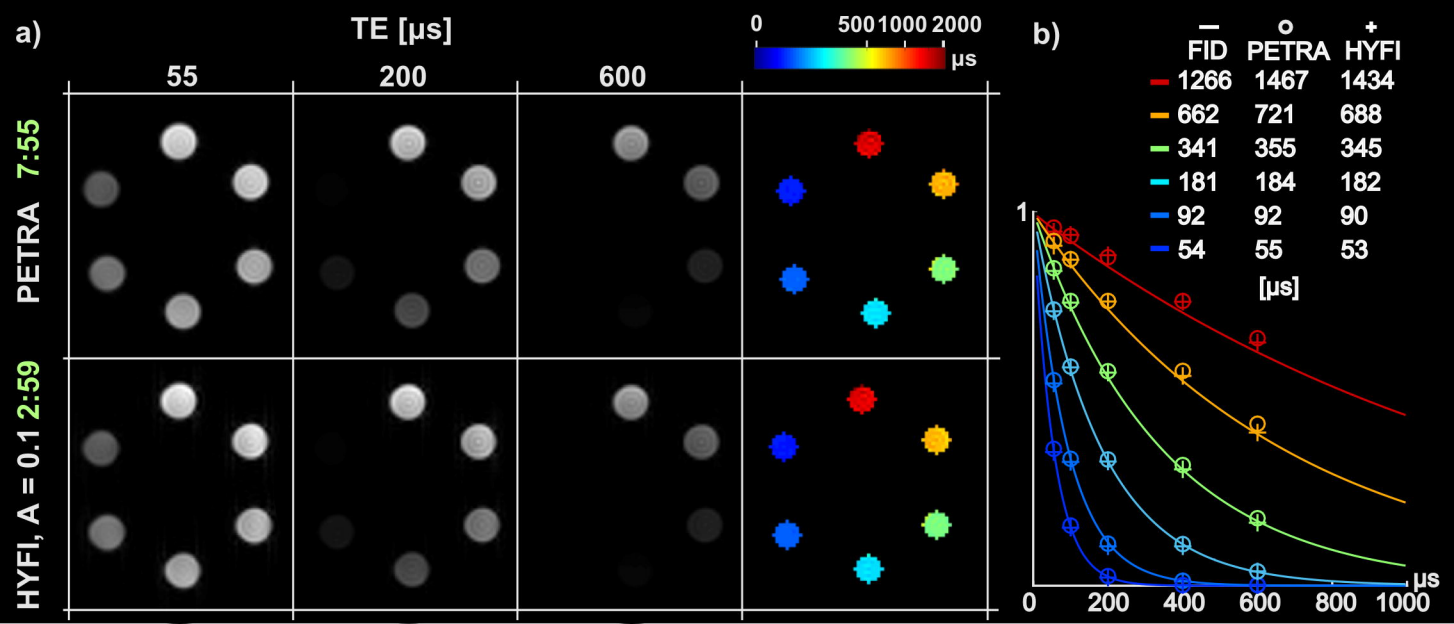
a)
TE [µs]
55
200
600
0
500 1000 2000
µs
PETRA 7:55
HYFI, A = 0.1 2:59
b)
FID
PETRA
HYFI
1266 1467 1434
662 721 688
341 355 345
181 184 182
92 92 90
54 55 53
[µs]
1
0
200
400
600
800
1000
µs